CHEMISTRY OF MATERIALS
Cite This: Chem. Mater. 2018, 30, 7100−7110
Article
pubs.acs.org/cm

Structure Dependent Phase Stability and Thermal Expansion of Ruddlesden−Popper Strontium Titanates

Liang-Feng Huang, Nathan Z. Koocher, Mingqiang Gu, and James M. Rondinelli*

Department of Materials Science and Engineering, Northwestern University, Evanston, Illinois 60208, United States

Supporting Information

ABSTRACT: Ruddlesden−Popper strontium titanates with composition $Sr_{n+1}Ti_nO_{3n+1}$, RP-*n*-STO, n = 1, 2, ..., ∞, are prototypical layered perovskites from which many crystal-chemistry principles can be assessed. In addition, their phase stabilities and lattice thermal expansions are essential factors for their usage in realistic devices. In this work, we use first-principles electronic structure methods to determine the *n*-layer dependent phase stabilities, including thermodynamic energies and pressure−critical temperature ($P-T_c$) phase diagrams and coefficients of thermal expansion. We correlate these properties with the perovskite $(SrTiO_3)_n$·SrO block thickness, n, to show that a change in materials behavior occurs at a critical thickness n_c = 3, which we ascribe to the presence (absence) of octahedral layers exhibiting antiferrodistortions at $n \geq 3$ ($n < 3$). Last, we attribute the absence of quasi-two-dimensional lattice anharmonicity in the layered RP titanates to the stiff $(SrTiO_3)_n$ intrablock Ti−O bonds and strong interblock bonding. The layer dependent properties studied here will be useful for the design and application of related quasi-2D materials and devices.

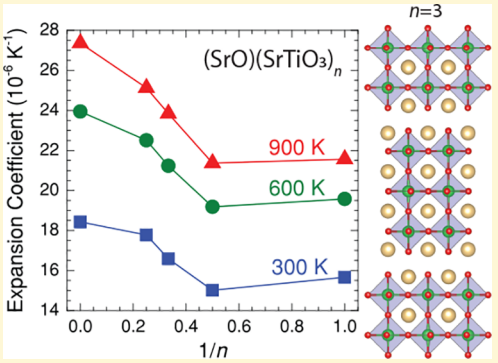

INTRODUCTION

Ruddlesden−Popper strontium titanates ($Sr_{n+1}Ti_nO_{3n+1}$, RP-*n*-STOs, n = 1, 2, ..., ∞) are a prototypical group of perovskites with well-known stable structures.[1] Numerous phenomena, including ferroelectricity, multiferroism, thermal and electronic transport behavior, and optical responses, have been comprehensively studied in various pristine and doped RP-STOs.[2−9] The phase stability and thermal expansion of RP-STOs are both important for integrating these functional materials into realistic devices and for understanding the effects of coupled physical responses, e.g., electron−phonon scattering due to soft polar phonons.

In perovskites, displacive phase transitions frequently occur with polymorphic transitions tuned by octahedral distortions (e.g., rotation and tilting), which offer a functional approach to design structure-derived perovskite properties (e.g., ferroelectricity and optics).[10−17] To exploit a certain superior physical property exhibited by one of the polymorphic phases requires that phase stability can be tuned. In this context, the thermodynamic properties of RP-STOs have been intensively studied by both experimental measurements and theoretical calculations for decades due to their high and general importance;[9,18−24] however, those previous results were mainly for RP-STOs without consideration of the role that octahedral distortions serve. Therefore, quantitative and systematical understandings of the thermodynamic behaviors of octahedral distortions at different intrinsic conditions (e.g., n) and extrinsic environments (e.g., temperature and stress) are still of broad necessity, which will also be helpful for exploring functional properties in RP-STOs as well as numerous related structural derivatives. Considering the relatively large uncertainty (≲0.5 eV) in the previous theoretical formation energies of RP-STOs (with respect to SrO and $SrTiO_3$, without thermal corrections) by different empirical models and ab initio methods,[18−23] thermodynamic phase diagrams based on such free energies, as well as their comparison with experimental observations, are required to establish a crystal-chemical understanding of the underlying energetics.

Thermal expansion is another critical factor determining the capability, performance, and lifetime of materials working under variable thermal conditions. For example, the Invar property (i.e., small/negligible thermal expansion) of Fe−Ni alloys makes them useful for precision instruments, e.g., watch-hair spring and micromachinery systems;[25,26] however, in multilayer ceramic coatings[27,28] and miniature transistors,[29−32] it is the thermal-expansion mismatch and the resulting internal thermal stress between the contacting components that cause severe cracks and spallations under thermal cycling. As an incipient ferroelectric material, ferroelectricity can be readily induced in $SrTiO_3$ by various approaches (e.g., electric field, stress, and chemical substitution),[33] and ferroelectric field-effect transistors made of substrate-supported perovskites (e.g., $SrTiO_3$) have also been fabricated and are promising for information storage and processing,[34,35] for which phase stability and thermal expansion are expected to be important during processing and in operation.

Received: July 12, 2018
Revised: September 25, 2018
Published: September 26, 2018

DOI: 10.1021/acs.chemmater.8b02944
Chem. Mater. 2018, 30, 7100−7110

The thermal-expansion mechanisms in perovskites have been studied for decades,[36,37] and this thermodynamic response is an effective macroscopic probe into the microscopic character of materials (e.g., lattice geometry, atomic coordination, bond strength, and phase stability).[38−45] Thermal expansion may correlate with structural transitions, and both phenomena can be effectively tuned by chemical approaches.[36,37,41,43,44] Structural transitions are also one of the three major mechanisms for realizing negative thermal expansion (NTE) in perovskites, of which the rigid-unit mode and electronic-structure transition mechanisms are the other two routes.[46] For layered RP perovskites, a quasi-two-dimensional vibration may also result in NTE, which was first reported in RP $Ca_3Ti_2O_7$, $Ca_3Zr_2O_7$, and $Sr_3Zr_2O_7$ under hydrostatic pressure.[46] In addition, the thermal expansion responses of perovskites were mostly studied by experimental measurements as first-principles simulations have been partly prohibited by the spurious imaginary modes appearing in the phonon spectra calculated within the density-functional theory (DFT) method.[46] This computational challenge both impedes assessing the complex microscopic mechanisms underlying the experimental observations and also limits predictive investigations on the thermal behaviors of many perovskites.

In this work, we study the distorted and undistorted phases of RP-*n*-STOs (n = 1, 2, 3, 4, ..., ∞) at pressures of 0−30 GPa and overcome the problem of spurious imaginary modes in the thermal-expansion simulations using our self-consistent quasi-harmonic (SCQHA) method.[47] In the structure dependent thermodynamic energies, $P-T_c$ phase diagrams, and thermal expansion coefficients, we identify a critical octahedral-block thickness, n_c = 3, where the thermodynamic responses of the titanates are found to originate in changes to the TiO_6 octahedral layers with antiferrodistortive rotations. We find no quasi-two-dimensional NTE in these layered RP-STOs, which is understood by analyzing their phonon anharmonicities and electronic structures.

MATERIALS AND METHODS

Structures. $SrTiO_3$ has two well-known phases,[1] i.e., the cubic phase ($Pm\bar{3}m$, space group no. 221) and the tetragonal phase ($I4/mcm$, no. 140). The $Pm\bar{3}m$ phase exhibits undistorted TiO_6 octahedra (Figure 1a,b) and is stable at temperatures $\gtrsim$105 K[33,48−52] under ambient pressure. The TiO_6 octahedra in the $I4/mcm$ phase exhibit out-of-phase antiferrodistortive TiO_6 rotations (Figure 1c,d), and this distorted phase is stable at temperatures $\lesssim$105 K.[33,50−52]

In RP-*n*-STOs (n = 1, 2, 3, 4, ...), the neighboring $(SrTiO_3)_n$ blocks with n octahedral layers are separated by a rock-salt SrO monolayer (Figure 2). One expects that upon increasing the $(SrTiO_3)_n$·SrO block thickness n, the structures, as well as various physical properties, of the RP-*n*-STOs should gradually approach those of bulk $SrTiO_3$ (n = ∞). To assess such a structural trend, we generate the structures of RP-*n*-STOs by extracting the $(SrTiO_3)_n$·SrO blocks from the parent $SrTiO_3$ lattice and assemble them to form different members of the n homologous RP series. There are two $(SrTiO_3)_n$·SrO blocks in each unit cell, with a relative translation of t ∼ 2.75 Å between layers (Figure 1b,c). The two parent $SrTiO_3$ lattices (i.e., the undistorted $Pm\bar{3}m$ and distorted $I4/mcm$ phases) result in the corresponding undistorted and distorted RP-*n*-STOs polymorphs. The undistorted RP-*n*-STOs exhibit the complete symmetry of $I4/mmm$ (no. 139), and the distorted ones exhibit *Cmce* (no. 64) symmetry for odd n (e.g., 1, 3, ...) and the *Ccce* (no. 68) symmetry for even n (e.g., 2, 4, ...).

Sr_2TiO_4 and $Sr_3Ti_2O_7$ only exhibit stable undistorted $I4/mmm$ phases,[1] and our DFT structural optimizations also spontaneously transform these distorted *Cmce* and *Ccce* phases into the ideal $I4/mmm$ structures. Although the stable *Pcab* (no. 61) phase has been found for RP $Ca_4Ti_3O_{10}$ (n = 3)[1] it is not observed in $Sr_4Ti_3O_{10}$ (n = 3). The *Pcab* structure slightly differs from the *Cmce* phase examined here by a small displacement (∼0.02 Å) of the alkaline-earth A-site cation. Such an A-cation displacement is not energetically favored in RP-3-STO, and a structural optimization by DFT converts the *Pcab* phase back to the *Cmce* polymorph. Different from the nonpolar RP-STO phases under hydrostatic pressures (0−30 GPa), a ferroelectric instability (i.e., polar RP-STOs) can be induced by epitaxial strain;[3,5] these strained-stabilized structures are not studied here but would be an interesting and important future research direction that would benefit from using similar thermodynamic and lattice-dynamical methods.

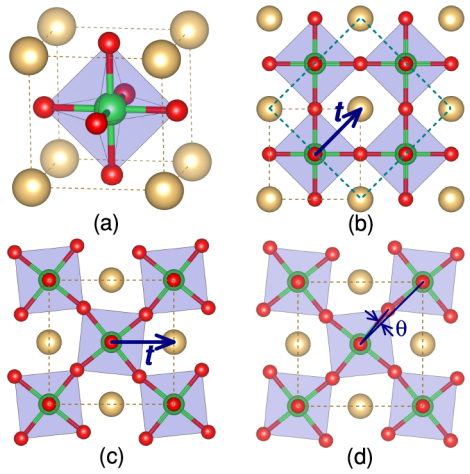

Figure 1. (a, b) The perspective and top views of the undistorted $Pm\bar{3}m$ phase of $SrTiO_3$ and (c, d) the top views of the two neighboring octahedral layers in the $I4/mcm$ phase of $SrTiO_3$, where the octahedral-rotation angle (θ) is labeled in panel d. In (b), the $\sqrt{2} \times \sqrt{2} \times 1$ periodic cell that accommodates the octahedral distortion (i.e., that in the $I4/mcm$ phase) is indicated. In (b, c), the arrows indicate the relative translations (t) between the neighboring $(SrTiO_3)_n$ blocks in the undistorted and distorted phases of RP-STOs, respectively.

Density Functional Theory (DFT) Simulations. The DFT calculations are performed using the Vienna *Ab Initio* Simulation Package.[53] The PBEsol functional[54,55] with a modified electronic potential for extended crystals is used to describe the electronic exchange and correlation. The projector augmented-wave method[56,57] is used to describe the electronic wave functions and Hamiltonians with both efficiency and accuracy. An 800 eV cutoff energy is used for expanding the electronic wave functions and charge densities in plane waves. For the numerical integration of the electronic states in the Brillouin zones, we used reciprocal k meshes of $\gtrsim \frac{24}{a_0} \times \frac{24}{b_0} \times \frac{24}{c_0}$, where a_0, b_0, and c_0 are lattice constants scaled by units of angstroms. The energy threshold for the self-consistent electronic convergence is 5×10^{-10} eV/atom, and the force and stress thresholds for the structural optimization are 10^{-3} eV/Å and 0.1 GPa, respectively.

To calculate accurate equation of states (EOS) for all of the involved volumes (V) at pressures ranging from 0 to 30 GPa and temperatures ranging from 0 to 900 K, we considered a large volume range of $\delta V/V_0 \in [-18\%, 9\%]$, where V_0 and δV are the equilibrium volume and the deviation from it, respectively. During the DFT optimization for each (pressurized) structure, the unit-cell volume is conserved, while the unit-cell shape and internal atomic coordinates are fully optimized. The discrete electronic energy−volume (E_e-V) relationships obtained from DFT calculations are then fit using an analytical five-parameter Birch−Murnaghan EOS.[58] See the Supporting Information for more details about the crystal structures and EOS fits.

DOI: 10.1021/acs.chemmater.8b02944
Chem. Mater. 2018, 30, 7100−7110

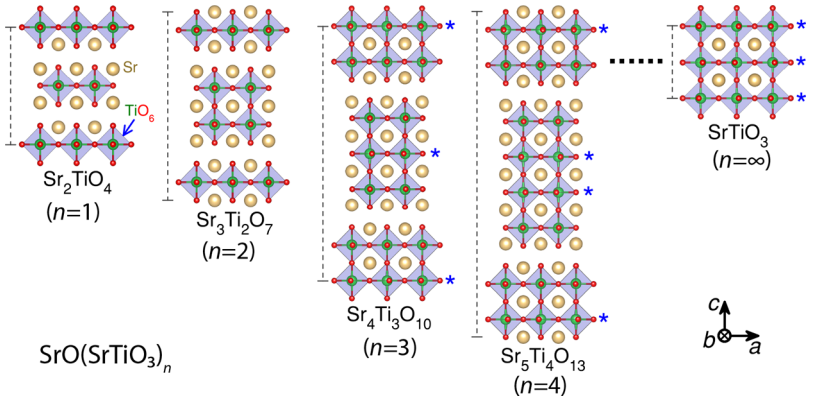

Figure 2. Crystalline structures of RP-*n*-STOs with the *c*-axes of the unit cells indicated by dashed lines and the octahedral layers in $Sr_4Ti_3O_{10}$, $Sr_5Ti_4O_{13}$, and $SrTiO_3$ exhibiting considerable antiferrodistortive rotations labeled with asterisks.

Phonon Spectra. The phonon spectra are calculated using the small-displacement method[59,60] which is implemented in the PHONOPY software package.[61] The atomic-displacement magnitude of 0.03 Å is used to calculate the force constants and phonon spectra. Our prior studies on bulk and nanoscale transition metal compounds show that the atomic forces exhibit a spatial extent l_c of $\lesssim$9 Å.[62,63] Thus, when we use supercells to obtain accurate force constants in the phonon calculations, we need to ensure the spatial sizes are sufficiently large (e.g., $\gtrsim l_c$), and the derived anharmonic properties like the thermal-expansion coefficients are reliable. We use only the ground-state structures in the thermal-expansion simulations and large supercells with spatial sizes of 11−36 Å: 4 × 4 × 2 supercell for *I*4/*mmm* Sr_2TiO_4 (448 atoms), 4 × 4 × 1 for *I*4/*mmm* $Sr_3Ti_2O_7$ (384 atoms), 2 × 2 × 1 for *Cmce* $Sr_4Ti_3O_{10}$ (272 atoms) and *Ccce* $Sr_5Ti_4O_{13}$ (352 atoms), and 2 × 2 × 2 of the *I*4/*mcm* polymorph for $SrTiO_3$ (160 atoms). To calculate the $P-T_c$ phase diagrams for RP-*n*-STOs at n = 3, 4, ∞, the phonon spectra and then the free energies of their high-temperature undistorted phases are simulated using relatively smaller supercells (8−36 Å), i.e., 2 × 2 × 1 for *I*4/*mmm* $Sr_4Ti_3O_{10}$ (136 atoms) and *I*4/*mmm* $Sr_5Ti_4O_{13}$ (176 atoms) and 2 × 2 × 2 for $Pm\bar{3}m$ $SrTiO_3$ (40 atoms).

Although there should be LO−TO splitting in the phonon spectra of RP-*n*-STOs originating from the nonanalytical corrections to the force constants in ionic crystals,[64,65] its contribution is unimportant in obtaining the thermodynamic properties of the material because only a small fraction of the phonon modes close to the Brillouin-zone center are affected by the correction.[47,66,67] Thus, LO−TO splitting is neglected here to simplify the already complex phonon spectra.

Thermal-Expansion Simulations. The thermal expansions of solids can be simulated using the quasi-harmonic approximation (QHA) method,[61,68] which makes it possible to obtain accurate thermodynamic data in an efficient way. In the conventional QHA method, the temperature dependent equilibrium volume is determined by minimizing the Gibbs free energy with respect to volume at each temperature.[47] For this purpose, the phonon spectra of about ten or more volumes are usually needed to obtain a precise free energy−volume relationship. However, in some oxides (e.g., TiO_2,[69−71] $SrTiO_3$,[33,72] $Ca_3Ti_2O_7$,[46,47] and Ca_2GeO_4[73]), there are spurious imaginary modes in the DFT phonon spectra for the stable phases at volumes $\gtrsim V_0$. Such issue in these oxides should originate from the delicate balance between the short-range repulsion and long-range electrostatic force therein,[69,74] which makes the thermodynamic and dynamical stabilities sensitive to many kinds of perturbations, e.g., stress, temperature, charge variation, electric field, chemical substitution, and even variations in the exchange-correlation functional used in the DFT method.[33,69,72,74] It is this imaginary-phonon problem that prohibits applying the conventional QHA method to these oxides. The complication also exists here for the layered RP titanates as seen in the phonon spectra of perovskite *I*4/*mcm* $SrTiO_3$ (Figure 3). More details about the imaginary modes in *I*4/*mcm* $SrTiO_3$ can be found in the Supporting Information, where we assess

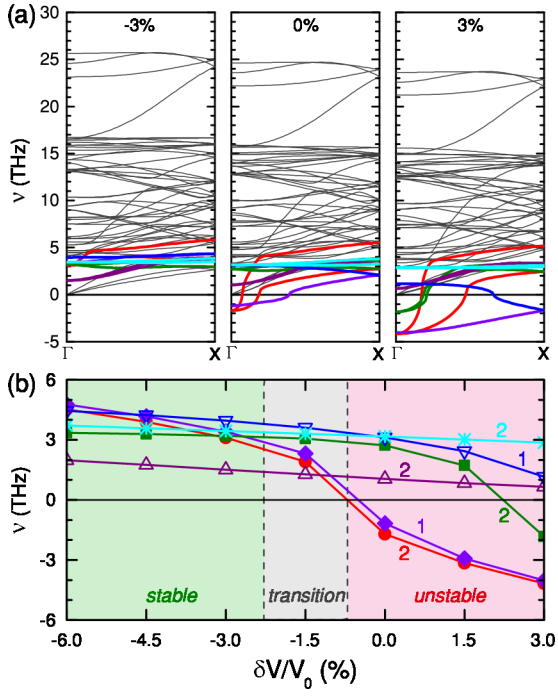

Figure 3. Phonon spectra and the ten lowest optical modes (at the Γ point) of *I*4/*mcm* $SrTiO_3$ at different volumes, where the negative sign indicates imaginary modes. The lowest ten optical modes are labeled by thick lines in (a), and their degeneracies (1 or 2) are indicated in (b). In (b), the regions with stable and unstable modes, as well as the intermediate transition region, are indicated.

the variations in the imaginary modes arising from different density functionals (i.e., LDA, PBE, and PBEsol) to show the spurious soft modes are due to the functional dependent volumes.

It is likely that the aforementioned spurious-lattice instability is the reason why there are limited theoretical studies on the thermal expansion behavior of the RP-STOs arising from phonon anharmonicity. The only reported study we could find is on the n = 1, 2, and ∞ RP-STOs, which combines DFT and an empirical Debye model.[75] However, the Debye model was originally formulated for materials with uniform atomic-bond characters across the lattices (e.g., metallic elements and alloys[58,76−80]), where the vibrational behaviors can be well described by acoustic-like modes. The Debye model is less rigorous for describing complex compounds with different types of chemical bonds and local structure anisotropy; therefore, its application to such materials requires careful assessment. Note that the unstable DFT phonons may be stabilized by phonon−phonon interactions (i.e., higher-order anharmonicity) at finite

DOI: 10.1021/acs.chemmater.8b02944
Chem. Mater. 2018, 30, 7100−7110

temperatures, which have been considered for the high-temperature cubic phase of $SrTiO_3$ at 300 K.[81,82] However, calculating the high-order anharmonicity remains computationally expensive today even for phonon spectra of the primitive unit cell with one formula unit; it would be challenging to obtain such interactions multiple times when calculating the thermal expansion coefficient of several RP-*n*-STOs, especially those with large n and large unit cells.

To efficiently avoid the spurious imaginary modes, we developed the self-consistent quasiharmonic approximation (SCQHA) method,[47] which has helped us obtain the first *ab initio* volume-thermal-expansion coefficient (α_V) of RP $Ca_3Ti_2O_7$,[46,47] which is in excellent agreement with experimental measurements.[83] In this method, the phonon spectra at any volume are extrapolated from the stable phonon spectra at three volumes using a second-order Taylor expansion as

$$\nu(V) = \nu(V_r) + \left(\frac{d\nu}{dV}\right)\delta V + \frac{1}{2}\left(\frac{d^2\nu}{dV^2}\right)\delta V^2 \quad (1)$$

where ν is the phonon frequency; V_r and δV are the reference volume and the deviation from it, respectively; the two Taylor coefficients in the expansion are calculated using the phonon spectra at the three chosen volumes. According to the $\nu-V$ relationships for the lowest ten optical modes in $I4/mcm$ $SrTiO_3$ (Figure 3b), we discern three distinct regions: (1) an *unstable region* with some imaginary modes at $\delta V/V_0 \gtrsim 0\%$, (2) a *stable region* with all modes having real and smooth $\nu(V)$ curves at $\delta V/V_0 \lesssim 3\%$, and (3) a *transition region* bridging the unstable and stable regions. In both the unstable and transition regions, there are highly nonlinear $\nu(V)$ curves. Only the smooth $\nu(V)$ curves in the stable region allow us to obtain well-behaved Taylor expansions. Thus, three volumes in the stable region are chosen to calculate the coefficients in eq 1.

The equilibrium volume at a given temperature (T) and external pressure (P) is calculated in a self-consistent way using the relationship[47]

$$V(P, T) = \left[\frac{dE_e(V)}{dV} + P\right]^{-1} \frac{1}{N_q}\sum_{q,\sigma} U_{q,\sigma}\gamma_{q,\sigma} \quad (2)$$

where $E_e(V)$ is the electronic energy−volume relationship described by the EOS; q and σ are index the phonon wavevector and branch, respectively; N_q is the total number points on the q grid ($\sim\frac{40}{a_0}\times\frac{40}{b_0}\times\frac{40}{c_0}$ here); and $U_{q,\sigma}$ and $\gamma_{q,\sigma}$ ($=-\frac{V}{\nu_{q,\sigma}}\frac{d\nu_{q,\sigma}}{dV}$) are the internal energy and Grüneisen parameter of the phonon mode (q, σ), respectively. During the calculation of $V(T)$, both the volume V and phonon frequency ν are iteratively solved using eqs 1 and 2 until the convergence threshold for V (10^{-6} Å^3) is reached, where a balance between the external pressure and the internal electronic and phononic pressures, $P = P_e(V) + P_{ph}(V,T)$, is implicitly achieved.[47] To calculate the Grüneisen parameters γ, similar phonon branches at different volumes are matched using an eigenvector orthonormality constraint,[84] which is also used to sort the phonon branches at different q coordinates. The volume-thermal-expansion coefficient is then directly calculated from the $V-T$ relationship as $\alpha_V = \frac{1}{V}\frac{dV}{dT}$.

We consider the volume expansion effects to understand better the structure dependent lattice dynamics of the RP-STOs, where the thermal-expansion anisotropy is only partially considered through the DFT optimization of the unit-cell shape at each volume. The internal coupling between different lattice vectors (i.e., Poisson ratio) may also be affected by phonon excitations at finite temperatures, which additionally contribute to the thermal-expansion anisotropy.[85] However, such internal coupling should not produce an observable change in the volume expansion,[86,87] and accurate thermal-expansion coefficients and other thermodynamic properties of various materials have been simulated using the SCQHA method[47] without considering the temperature dependent Poisson ratio.

RESULTS AND DISCUSSION

Phase Stabilities. To quantitatively understand the structure dependent stabilities of the RP-STOs, as well as the behaviors and effects arising from octahedral rotations, we use two forms of formation energies:

$$E_f = E_e(\text{RP-}n\text{-STO}) - (n+1)E_e(\text{SrO}) - nE_e(TiO_2) \quad (3)$$

and

$$E_f^* = E_e(\text{RP-}n\text{-STO}) - E_e(\text{SrO}) - nE_e(SrTiO_3) \quad (4)$$

where different sets of reference materials are used for E_f and E_f^*, respectively. E_f indicates the thermodynamic stability of RP-*n*-STO with respect to the reactant binary oxides (SrO and TiO_2), whereas the n dependent E_f^* can discern the interaction between neighboring SrO monolayers (distance $d \sim 4.48{\cdot}n$ Å) in the RP titanates. Both E_f and E_f^* have also been frequently used in previous theoretical studies to indicate the relative stabilities between different RP-STOs or those of planar RP defects in perovsite $SrTiO_3$.[18−23] To validate the high accuracy of our DFT method, we further compute the thermal corrections to the formation energies, and the obtained temperature dependent free energies of formation for RP-STOs that closely agree with many available experimental data[24] (see section F of the Supporting Information).

Our calculated variations of E_f (in eV/atom) and E_f^* (in eV/f.u.) with respect to inverse layer thickness, $1/n$, are shown in Figure 4a. For $n \leq 2$, both formation energies show that the undistorted $I4/mmm$ phase is only stable. This can be readily seen from the difference in E_f (δE_f, meV/atom) between the ground-state phase and the $I4/mmm$ phase, as shown in the inset of Figure 4a. The stability is due to the presence of only *interfacial octahedral layers* directly bonded with the rock-salt SrO monolayers at the interfaces between $(SrTiO_3)_n$ blocks (Figure 2); these interlayer interactions can tune the rumpling[4] of the monoxide layers and energetically disfavors octahedral rotations. However, at $n \geq 3$, there are additional perovskite-like *internal octahedral layers* (labeled with asterisks in Figure 2) sandwiched between the interfacial layers, and the octahedral rotation in the internal layers supports the stability of the distorted *Cmce* and *Ccce* phases with lower electronic energies than the undistorted $I4/mmm$ phase.

In addition, we find that E_f becomes more negative with decreasing $1/n$ (i.e., approaching the $SrTiO_3$ stoichiometry), indicating the enhanced stability of the thicker layered RP-*n*-STO with respect to the binary SrO and TiO_2 oxides. The energetic trend with respect to inverse thickness $1/n$, however, changes at $n = 3$ ($Sr_4Ti_3O_{10}$), discernible in the $\delta E_f(1/n)$ data but not as obvious in the $E_f(1/n)$ curve. The ground-state E_f^* also decreases with decreasing $1/n$, indicating the repulsive interaction between SrO monolayers within the $SrTiO_3$ lattice. Such inter-SrO-layer repulsion is assisted by the octahedral rotations for values of $n \geq 3$, and it becomes attractive for the undistorted lattices at $n \geq 3$, resulting in the lowest E_f^* for the undistorted phase at $n = 3$ (inter-SrO-layer distance ~13.5 Å).

A similar transition at $n = 3$ is also seen in other properties, including the DFT bulk modulus (B_0, Figure 4b) obtained from our EOS parametrization, as well as the band gap (shown in the Supporting Information). B_0 increases with decreasing $1/n$ because of the increased ratio of covalent (stiffer) Ti−O bonds, which exceeds a critical number density in the RP structure as seen by the change in slope at $n = 3$. The

DOI: 10.1021/acs.chemmater.8b02944
Chem. Mater. 2018, 30, 7100−7110

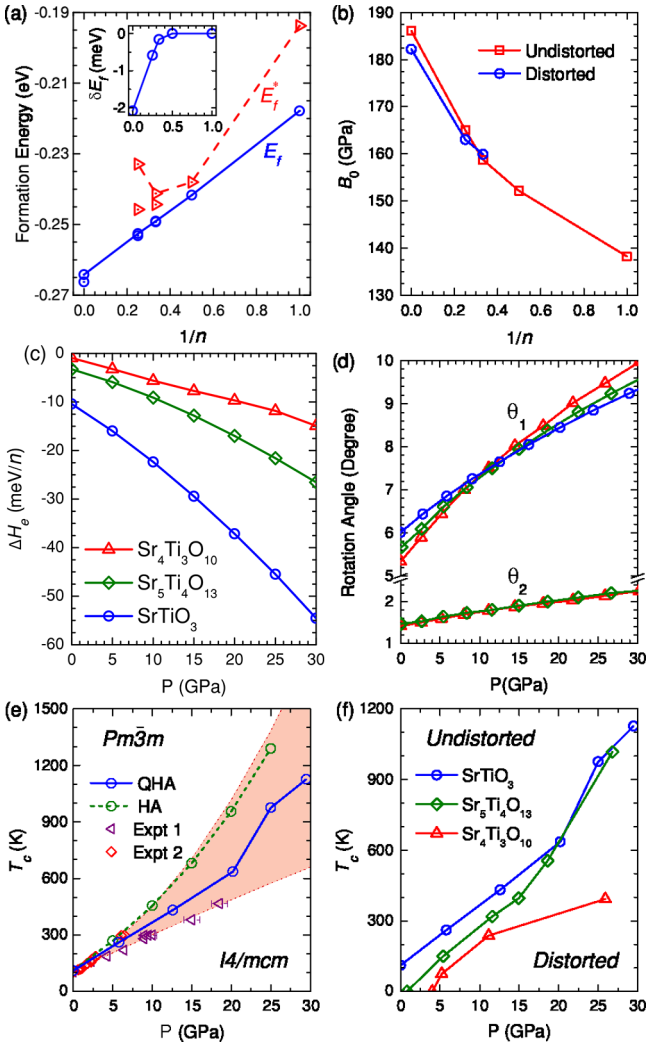

Figure 4. (a) Formation energies (E_f per atom and E_f^* per formula unit), (b) DFT bulk modulus (B_0), (c, d) pressure dependent relative electronic enthalpy (ΔH_e between distorted and undistorted phases) and octahedral-rotation angles (θ_1 and θ_2), (e) $P-T_c$ phase diagram for $SrTiO_3$ ($n = \infty$) with the experimental data[50,51] provided for comparison, and (f) $P-T_c$ phase diagrams for RP-n-STOs (n = 3, 4, ∞). In the main panel of (a), the lines connect the undistorted phases, and the inset shows the relative E_f (δE_f) between the ground state and undistorted phase.

simultaneous occurrence of the above structure dependent stabilities and stiffnesses for the RP-STOs indicate a common critical dimensionality change at $n = 3$, which divides the RP-n-STOs into two groups with $n < 3$ and $n \geq 3$. We expect that similar structural trends may also exist in other thermodynamic and lattice-dynamical properties.

We next show that hydrostatic pressure can be used as an effective approach to tune the octahedral-rotation angle (θ) and phase stabilities for the distorted RP-n-STO phases with $n \geq 3$. The pressure dependent relative enthalpies (ΔH_e) of the distorted RP-n-STO (n = 3, 4, ∞) with respect to their undistorted counterparts are shown in Figure 4c, and the octahedral-rotation angles of the internal (θ_1) and interfacial (θ_2) octahedral layers are shown in Figure 4d. The monotonic stabilizing effect of P on the distorted phases, i.e., decreasing ΔH_e with increasing P, and the monotonic increasing trends in θ_1 and θ_2 are clearly observed. The distorted phase of a RP-n-STO with a larger n (i.e., more internal octahedral layers) both has a higher phase stability (i.e., lower ΔH_e) and also a more significant pressure-stabilizing tendency (i.e., greater $\frac{d\Delta H_e}{dP}$ slope). The values of θ_1 also increase very quickly with increasing pressure, indicating the sensitive response of the internal octahedral layers to the pressure, while the corresponding θ_2 values for the interfacial octahedral layers exhibit smaller amplitudes and weaker pressure dispersions. In contrast, we find the titanates with $n \leq 2$ remain undistorted for all pressures (P) up to 30 GPa, which we attribute to the insufficient number of internal octahedral layers which break the coherency preference of the cooperative octahedral tilt pattern.

Experimentally, the reported pressure stabilizing effect on the distorted phase should be indirectly reflected by the variations in θ_1 and θ_2, which can be quantitatively detected by measuring the pressure dependent structural transition[50,51,88] between the distorted (a low-temperature) phase and the undistorted (a high-temperature) phase. In the following, the relationship between the imposed pressure P and the critical temperature T_c for the thermally driven displacive phase transition is simulated using approaches within the harmonic and quasi-harmonic approximations (HA and QHA, respectively). Here we note that the QHA method also has been recently used to simulate the phase diagrams of electronic defects in $SrTiO_3$[89] and magnetic $BiCoO_3$,[90] justifying its application to the layered RP phases.

At the specified P and T, the relative stabilities between different phases are described by their change in Gibbs free energy

$$\Delta G(P, T) = \Delta H_e(P) + \Delta F_{ph}(V(P), T) \quad (5)$$

where ΔF_{ph} is the differential vibrational Helmholtz free energy, and the critical transition temperature T_c at each P is located by the condition that $\Delta G = 0$. The ΔH_e-P relationship is obtained from EOS fitting, and the $F_{ph}-P$ relationship is derived from the phonon spectra at different volumes (i.e., the QHA method). In the HA method, the volume dependence of F_{ph} is neglected, and the $F_{ph}(T)$ at the DFT equilibrium volume V_0 is used for the thermal effect at any pressure. In the high-temperature undistorted phases (e.g., $SrTiO_3$[33,72,91]), the lattice instability at low temperature results in some imaginary modes appearing in their DFT phonon spectra. As described above, such dynamical instabilities can be excluded by considering the high-order anharmonicity at sufficiently high temperatures,[81,82] which is computationally demanding to calculate. Alternatively, we use an efficient numerical treatment that simply omits the imaginary modes in the calculation of F_{ph}, which yields an accurate $P-T_c$ phase diagram for $n = \infty$ perovskite $SrTiO_3$ (as discussed below).

The simulated HA and QHA $P-T_c$ phase diagrams for $SrTiO_3$ are shown in Figure 4e, which are also compared to the available experimental data reported over the past few decades.[48−52] Although there is some quantitative discrepancies among the experimental data, they generally fall within two groups with remarkably different dT_c/dP slopes. According to the measured $P-T_c$ curves,[50,51] these two groups of experimental data (i.e., "Expt 1" and "Expt 2", Figure 4e) are fit to second-order polynomials, which form the lower and upper bounds on all of the experimental data. Such uncertainty in the experimental phase boundaries may be related to the ubiquitous hysteretic nature of the phase transitions observed

DOI: 10.1021/acs.chemmater.8b02944
Chem. Mater. 2018, 30, 7100−7110

in related ceramics (e.g., RP $Ca_3Mn_2O_7$[83] and metallic Ti alloys[92]). The simulated T_c at ambient pressure (~0 GPa) is 111 K, which is very close to the experimental value (105−110 K). The HA $T_c(P)$ curve is close to the upper experimental bound, and the QHA $T_c(P)$ curve resides between the upper and lower experimental bounds indicating a high degree of computational modeling accuracy for $SrTiO_3$, especially by the QHA method.

The QHA $T_c(P)$ curves for $Sr_4Ti_3O_{10}$, $Sr_5Ti_4O_{13}$, and $SrTiO_3$ are compared in Figure 4f, and the HA ones are given in the Supporting Information. There are some interesting trends observed in the QHA $P-T_c$ phase diagrams, which we itemize below:

(i) All of the dT_c/dP slopes are positive, which is consistent with a general rule that the sign of the dT_c/dP slope will be positive for perovskites when the octahedra (here TiO_6) are sufficiently stiff[88] owing to the covalent Ti−O bonds.

(ii) The critical temperatures for the homologous series follow a rank order such that $T_c(n = 3) < T_c(n = \infty)$, which is due to the same rank order identified for the stability of the distorted-phase titanate phases, i.e., the reverse order in ΔH_e (Figure 4c).

(iii) The $T_c(n = 4)$ resides between that of $n = 3$ and ∞ at $P < 20$ GPa, mainly due to the intermediate $\Delta H_e(n = 4)$ value (Figure 4c); however, $T_c(n = 4)$ approaches $T_c(n = \infty)$ for $P > 20$ GPa, indicating an important role of the pressure dependence in the vibrational Helmholtz free energy, F_{ph}.

In addition to using cation substitution to control T_c and the dT_c/dP slope,[43,52,88] we identified here how the n-layer dependence of the perovskite building blocks in the RP structures can be used to effectively tune the thermodynamic responses. Considering that many material properties rely on structural dependencies which change across structural phase transitions, our reported structure dependent thermodynamic stability should be useful for the design and application of related layered perovskites with non-d^0 transition metal cations under realistic conditions.

Furthermore, in the $P-T_c$ phase diagrams of $Sr_4Ti_3O_{10}$ and $Sr_5Ti_4O_{13}$ (Figure 4f), we find the undistorted phase is stable at 0 K and 0 GPa. However, the distorted polymorphs exhibit lower electronic energies at 0 GPa (i.e., $\Delta H_e < 0$, Figure 4c). These contrasting stabilities from ΔG and ΔH_e clearly reveal the important quantum-mechanical destabilizing effect of zero-point vibrations on the distorted phases. Such quantum-vibrational destabilizing effects in $Sr_4Ti_3O_{10}$ and $Sr_5Ti_4O_{13}$ will be overtaken by the stabilizing baric effect at $P > 4$ and >1 GPa (Figure 4f), respectively.

Thermal Expansions. The volume-thermal-expansion coefficients (α_V) for RP-n-STOs (n = 1, 2, 3, 4, ∞) at P of 0−30 GPa are shown in Figure 5, where the undistorted $I4/mmm$ phase is considered for n = 1 and 2, and the distorted $Cmce$, $Ccce$, and $I4/mcm$ polymorphs are used for the n = 3, 4, and ∞ phases, respectively. Note that for $n \geq 3$ the undistorted phases ($I4/mmm$ and $Pm\bar{3}m$) exhibit unstable DFT phonon spectra, prohibiting the simulation of thermal expansion in the QHA. The available experimental results for Sr_2TiO_4[93,94] and $SrTiO_3$[95,96] at the ambient pressure (~0 GPa) are also provided for comparison. The α_V values of $I4/mcm$ $SrTiO_3$ at 0 GPa diverge upon heating from 0 K owing to its instability at $T \gtrsim 105$ K, as shown in our $P-T_c$ phase diagram (Figure 4f). A similar phase instability (or low stability) of the distorted $Cmce$ $Sr_4Ti_3O_{10}$ and $Ccce$ $Sr_5Ti_4O_{13}$ occurs at low pressures (Figure 4f), which makes it impossible to obtain meaningful α_V values at $P \sim 0$ GPa using the (SC)QHA method. For this reason, we present α_V values for pressures ≥5 and ≥8 GPa for $Sr_4Ti_3O_{10}$ and $Sr_5Ti_4O_{13}$ in Figure 5c,d, respectively.

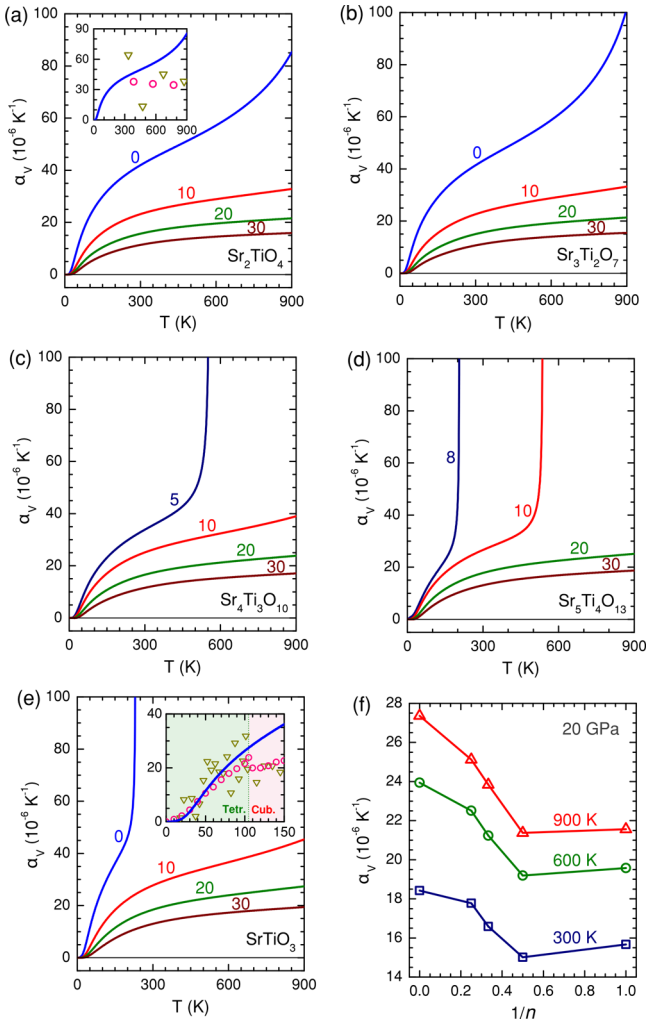

Figure 5. (a−e) Pressure dependent thermal expansion $\alpha_V(T)$ of the RP-STOs and (f) the variation of α_V (P = 20 GPa, T = 300−900 K) with layer thickness $1/n$. In the insets of (a) and (e), the available experimental data for Sr_2TiO_4[93,94] and $SrTiO_3$[95,96] at ambient pressure are provided, respectively. In the inset of (e), the $SrTiO_3$ tetragonal-cubic phase boundary at 105 K is indicated, and the theoretical α_V curve for tetragonal phase is meaningful below 105 K.

The simulated volume-thermal-expansion coefficient for $I4/mcm$ $SrTiO_3$ (Figure 5e) agrees well with the measured experimental data below 105 K, above which the phase transition into the $Pm\bar{3}m$ phase results in a sudden decrease in the experimental α_V. This theory−experiment agreement for the α_V of $I4/mcm$ $SrTiO_3$ demonstrates the high accuracy of our SCQHA method and supports its application to the RP-STOs for which many do not have experimentally determined volume-thermal-expansion coefficients. The simulated α_V for $I4/mmm$ Sr_2TiO_4 (Figure 5a) is close to the experimental data at 300 K. However, upon heating, the experimental α_V values generally decrease and deviate more and more away from the theoretical $\alpha_V(T)$ curve which increases with T. This disagreement between the simulated and experimental data

DOI: 10.1021/acs.chemmater.8b02944
Chem. Mater. 2018, 30, 7100−7110

for $I4/mmm$ Sr_2TiO_4 is probably due to some technical issues in the experiments, which we discuss further next.

The thermal-expansion coefficient ($\alpha_V = \frac{1}{V}\frac{dV}{dT}$) can be re-expressed as[47]

$$\alpha_V = \frac{1}{N_q V B_T}\sum_{q,\sigma} c_{q,\sigma}\gamma_{q,\sigma} = \frac{1}{N_q V B_T}\int_0^{\nu_m} c(\nu)g(\nu)\,d\nu \quad (6)$$

where B_T is the isothermal bulk modulus, which consists of electronic and phononic contributions ($B_T = B_e + B_{ph}$); $c_{q,\sigma}$ is the isovolume heat capacity of the (q, σ) phonon mode; and ν_m is the maximum phonon frequency. There is only positive thermal expansion observed here for Sr_2TiO_4 because its phonon modes are fully dominated by those having positive Grüneisen parameters (γ), resulting in the fully positive γ-weighted phonon density of states (g_γ). This can be directly observed in the g_γ spectra and γ dispersions of Sr_2TiO_4 presented in Figure 6a. Owing to the excitation of more

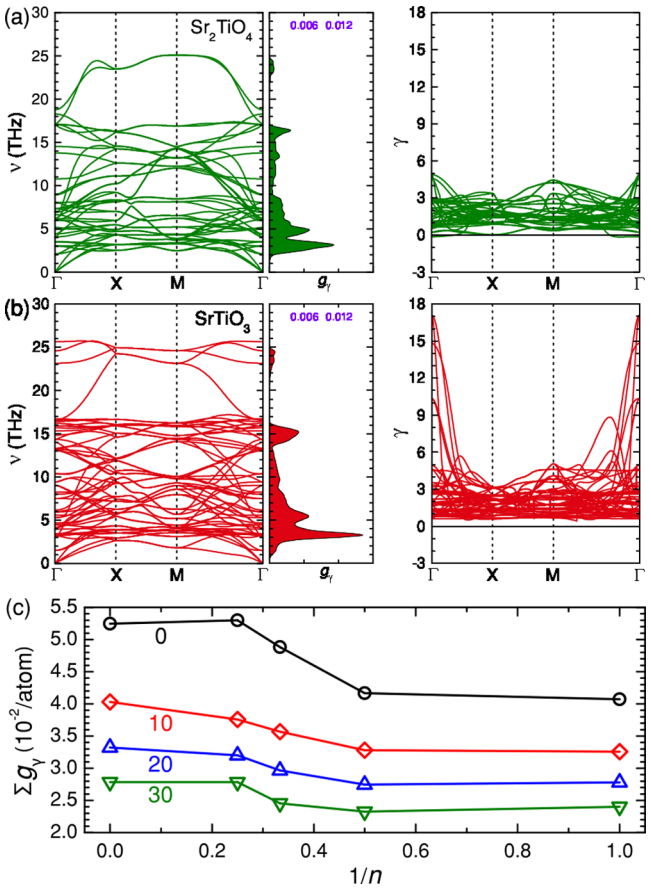

Figure 6. (a, b) Phonon dispersions, Grüneisen-parameter-weighted density of states (g_γ), and Grüneisen-parameter dispersions of Sr_2TiO_4 and $SrTiO_3$. (c) Integrations of g_γ ($\sum g_\gamma$) for RP-n-STOs at different pressures.

positive-γ modes with increasing temperature, the α_V of Sr_2TiO_4 should increase according to eq 6, as shown in the simulated $\alpha_V(T)$ curves (Figure 5). Therefore, the unexpected decreasing trend in the experimental α_V upon heating may indicate some unknown thermal processes happening in the experimental samples, e.g., the generation/annihilation of intrinsic defects and accumulation of thermal stresses between crystalline grains. Which features are the main culprits in this unusual decrease in α_V requires further experimental and theoretical investigations. If any unexpected extrinsic or microstructural processes are found to affect α_V in the future, we expect that the quality of single-crystal perovskite samples can be efficiently assessed by measuring the α_V data. Last, we note that the available experimental α_V data for Sr_2TiO_4 were measured using very large temperature steps ($\delta T \sim 200$ K) between sequential characterizations, and a smaller thermal step size (e.g., $\delta T \sim 10$ K as used for $SrTiO_3$[95,96]) should be preferred to exclude any possible technical apparatus sources for the unusual experimental trend.

Now we examine the pressure dependent volume-thermal-expansion coefficient of the RP-n-STO phases. As expected,[46,47] all of the α_V curves decrease with increasing pressure at any temperature (Figure 5a–e) because pressurization usually tends to enhance the bulk modulus (see the Supporting Information for B_T dependencies) and suppress the lattice anharmonicity (see Figure 6c for $\sum g_\gamma$), resulting in the suppressed α_V (by eq 6). On the other hand, the diverging $\alpha_V(T)$ curves for *Cmce* $Sr_4Ti_3O_{10}$, *Ccce* $Sr_5Ti_4O_{13}$, and $I4/mcm$ $SrTiO_3$ at low pressures (Figure 5c–e) are caused by the mechanical instabilities of those phases; i.e., B_T diverges with increasing T (see the Supporting Information). Stable volume-thermal-expansion coefficients for all RP-STOs are only observed at $P \gtrsim 20$ GPa. For that reason, we focus on volume-thermal-expansion coefficients at 20 GPa and different temperatures (e.g., 300, 600, and 900 K) to understand the structure dependent thermal expansion (Figure 5f). At each temperature, with increasing n (decreasing $1/n$), α_V exhibits a remarkable sudden increase at $n = 3$ and then saturates, approaching that of perovskite $SrTiO_3$. This behavior suggests that $n = 3$ corresponds to a critical structure for α_V and the role of the internal octahedral layers vis-á-vis octahedral distortions in enhancing the lattice anharmonicity. Such an anharmonicity-enhancing effect of the octahedral rotations, for example, can also explain the sudden decrease in the α_V of $SrTiO_3$ during its tetragonal–cubic phase transition at ~105 K (Figure 5e, inset), where the antiphase octahedral rotations about the c-axis are eliminated upon heating. This mechanism can be further generalized to explain the enhanced α_V value of ScF_3 nanoparticles arising from the compressive surface stress,[45] which increases with decreasing particle size and induces octahedral distortions.

The effect of the perovskite-like blocks and internal TiO_6 layers can be further demonstrated by examining the structure dependent γ spectra, g_γ, and $\sum g_\gamma$ shown in Figure 6. From eq 6, it can be derived that at high enough temperatures ($c_{q,\sigma} \sim k_B$), α_V will be proportional to $\sum g_\gamma$. As seen from the isovolume heat capacities of RP-STOs (see the Supporting Information), most of the phonon modes in the RP-STOs can be readily excited at relatively low temperatures (e.g., 50% at 130 K and 81% at 300 K), making the summation $\sum g_\gamma$ an efficient descriptor to understand many trends in the thermal expansion behavior. As shown in Figure 6a,b, $SrTiO_3$ (with all the TiO_6 octahedra rotated) generally has higher γ and g_γ than those of Sr_2TiO_4 (without any TiO_6 octahedral rotations), indicating the enhancement of lattice anharmonicity by the octahedral tilt system. Such mechanism is further demonstrated by the common sudden increase in both α_V (Figure 5f) and $\sum g_\gamma$ (Figure 6c) at $n = 3$. The much higher sensitivity of θ_1 to volume change than that of θ_2 (Figure 4d) indicates that the atomic bonds in the distorted internal octahedral layers should have a greater volume dependence than those in the

DOI: 10.1021/acs.chemmater.8b02944
Chem. Mater. 2018, 30, 7100–7110

undistorted interfacial layers, which explains the enhanced lattice anharmonicity by octahedral distortion.

In addition to the thermal expansions of RP-STOs that are dependent on pressure, temperature, and n, the fully positive α_V for all pressures merits explanation as negative thermal expansions (NTE) can be triggered in other $n = 2$ layered RP perovskites, e.g., $Ca_3Ti_2O_7$ and $Sr_3Zr_2O_7$, by pressure.[46] Such NTE in those materials originates from the quasi-two-dimensional (quasi-2D) vibrational modes that have considerably negative Grüneisen parameters at 0 GPa, and the *membrane mechanism* (or the so-called *guitar-string mechanism* for quasi-one-dimensional cases),[46,97] which allows pressure to enlarge the negative γ values, resulting in observable NTE. It has been proposed that weaker interfacial bonding and softer octahedral layers may favor the appearance of quasi-2D lattice anharmonicity in layered perovskites.[46] Thus, transmuting these NTE layered-RP phases through the substitution of the A-site Ca cation (B-site Zr cation) with Sr (Ti) changes these two factors and eliminates any quasi-2D NTE in RP-STOs.

Next, we explore the chemical effects of cation substitutions on the interatomic bonding and lattice dynamics by examining the electronic density (ρ) of $n = 2$ $Sr_3Ti_2O_7$ with respect to the densities of $Ca_3Ti_2O_7$ and $Sr_3Zr_2O_7$. This allows us to understand better how the chemistry of the A and B cations affects the NTE independent of the structural degrees of freedom; i.e., we hold the $n = 2$ atomic structure fixed. The projection of ρ onto the z direction (ρ_z, z is along the c-axis) is calculated using

$$\rho_z(z) = \frac{1}{N_{xy}} \int \rho(\mathbf{r})\, dx\, dy \tag{7}$$

where N_{xy} is the number of numerical-grid points on the XY plane (i.e., the ab plane where c is the long crystallographic axis). The ρ_z of $Sr_3Ti_2O_7$ and its differences ($\Delta\rho_z$) with those of $Ca_3Ti_2O_7$ and $Sr_3Zr_2O_7$ (with the same atomic positions) are shown in Figure 7. The three-dimensional distributions of the differential charge density $\Delta\rho(\mathbf{r})$ are give in the Supporting Information. Positive $\Delta\rho_z$(STO-CTO) at the interfacial SrO monolayers indicates enhanced interfacial bonding in STO compared to that in CTO; thus, the disappearance of the quasi-2D NTE after substituting Ca with Sr arises from the strengthened interfacial bonding between monoxide layers. This increased bonding makes it more difficult to activate the Z-acoustic mode in the crystal largely responsible for the NTE.[46] The $\Delta\rho_z$(STO-SZO) is nearly zero at the interface, indicating that the interfacial bonding is largely unchanged with transition metal substitution at sites different from the monoxide layer (SrO). The $\Delta\rho_z$(STO-SZO) is large and positive at the B-site (i.e., Ti or Zr), indicating less electron loss from the B-site cation after Zr substitution with Ti. It tends to increase the covalency (decrease the ionicity) of the B−O bond and then stiffen the octahedral layer. Thus, the disappearance of quasi-2D NTE after substituting Zr with Ti is due to the more rigid octahedral layer, which limits the ability of the TiO_6 layer to buckle.

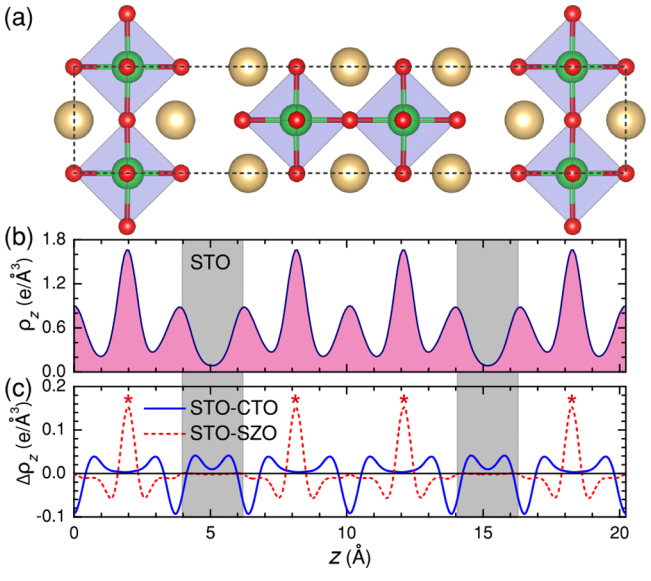

Figure 7. (a, b) Unit cell of $Sr_3Ti_2O_7$ and the z-direction projected (ρ_z) electron density. (c) Differential ρ_z distributions of $Sr_3Ti_2O_7$ (STO) with respect to $Ca_3Ti_2O_7$ (CTO) and $Sr_3Zr_2O_7$ (SZO). The shaded areas indicate the interfaces between octahedral blocks, and the asterisks indicate the Ti-atom positions.

CONCLUSION

In summary, we studied the phase stabilities and volume-thermal-expansion coefficients of Ruddlesden−Popper strontium titanates (RP-n-STO, n = 1, 2, 3, 4, ∞) using first-principles calculations. First, we identified that $n = 3$ corresponds to a structure with critical layer n_c where variations in the formation energies, $P-T_c$ phase diagrams, phonon properties, and thermal expansion occur. We attribute the crossover from quasi-2D to 3D materials behavior as arising from internal octahedral perovskite layers with antiferrodistortive rotations, which appear for strontium titanate polymorphs with $n \geq 3$. Our simulated $P-T_c$ phase diagram for perovskite $SrTiO_3$ is consistent with experimental measurements, and the obtained structure dependent diagrams of the RP-n-STOs will be useful for controlling polymorphic stability and their derived physical properties. Next, we simulated the thermal expansion of $SrTiO_3$ and found it agrees well with measured experimental data; however, the simulated α_V for Sr_2TiO_4 deviates from the experimental values, which we attribute to complexities in the experimental samples or characterization. Last, we found the quasi-2D lattice anharmonicity, which would support NTE in RP-n-STOs, to be negligible owing to both the strong interoctahedral-block bonding and high octahedral-layer stiffness in the $Sr_{n+1}Ti_nO_{3n+1}$ family. Considering that RP-n-STOs are a prototypical group of perovskites, the simulated results, proposed microscopic mechanisms, and the applied simulation/analysis strategy can be extended to understand the materials chemistry of other perovskite families exhibiting property dependent homologous series.

ASSOCIATED CONTENT

Supporting Information

The Supporting Information is available free of charge on the ACS Publications website at DOI: 10.1021/acs.chemmater.8b02944.

Additional structural details, equation of states, electronic structures, mode analyses, harmonic $P-T_c$ phase diagrams, temperature dependent bulk moduli, isovolume heat capacities, and electron densities for Ruddlesden−Popper strontium titanates (PDF)

DOI: 10.1021/acs.chemmater.8b02944
Chem. Mater. 2018, 30, 7100−7110

AUTHOR INFORMATION

Corresponding Author

*E-mail: jrondinelli@northwestern.edu (J.M.R.).

ORCID

Liang-Feng Huang: 0000-0003-2937-5183
James M. Rondinelli: 0000-0003-0508-2175

Notes

The authors declare no competing financial interest.

ACKNOWLEDGMENTS

L.-F.H. thanks Dr. D. Puggioni and Mr. D. Hickox-Young for helpful discussions on the physics of ferroelectricity in perovskites. L.-F.H. was supported by the ONR MURI "Understanding Atomic Scale Structure in Four Dimensions to Design and Control Corrosion Resistant Alloys" under Grant N00014-16-1-2280. N.Z.K. and M.G. were supported by the U.S. Department of Energy (DOE-BES) Grant DE-SC0012375. J.M.R. was supported by an Alfred P. Sloan Foundation fellowship (Grant FG-2016-6469). Calculations were performed using the QUEST HPC facility at Northwestern, the HPCMP facilities at the Navy DSRC, the HPC facility at the Extreme Science and Engineering Discovery Environment (NSF, ACI-1548562), and the CARBON cluster at Argonne National Laboratory (DOE-BES, DE-AC02-06CH11357).

REFERENCES

(1) Belsky, A.; Hellenbrandt, M.; Karen, V. L.; Luksch, P. New developments in the Inorganic Crystal Structure Database (ICSD): accessibility in support of materials research and design. *Acta Crystallogr., Sect. B: Struct. Sci.* **2002**, *58*, 364−369.

(2) Lee, K. H.; Kim, S. W.; Ohta, H.; Koumoto, K. Ruddlesden-Popper phases as thermoelectric oxides: Nb-doped $SrO(SrTiO_3)_n$ (n = 1,2). *J. Appl. Phys.* **2006**, *100*, 063717.

(3) Lee, J.; Arias, T. A. Structural phase transitions in Ruddlesden-Popper phases of strontium titanate: Ab initio and modulated Ginzburg-Landau approaches. *Phys. Rev. B: Condens. Matter Mater. Phys.* **2010**, *82*, 180104.

(4) Birol, T.; Benedek, N. A.; Fennie, C. J. Interface Control of Emergent Ferroic Order in Ruddlesden-Popper $Sr_{n+1}Ti_nO_{3n+1}$. *Phys. Rev. Lett.* **2011**, *107*, 257602.

(5) Lee, C.-H.; et al. Exploiting dimensionality and defect mitigation to create tunable microwave dielectrics. *Nature* **2013**, *502*, 532−536.

(6) Reshak, A. H. Thermoelectric properties of $Sr_{n+1}Ti_nO_{3n+1}$ (n = 1, 2, 3, ∞) Ruddlesden-Popper Homologous Series. *Renewable Energy* **2015**, *76*, 36−44.

(7) Reyes-Lillo, S. E.; Rangel, T.; Bruneval, F.; Neaton, J. B. Effects of quantum confinement on excited state properties of $SrTiO_3$ from ab initio many-body perturbation theory. *Phys. Rev. B: Condens. Matter Mater. Phys.* **2016**, *94*, 041107.

(8) Wang, H.; Su, W.; Liu, J.; Wang, C. Recent development of n-type perovskite thermoelectrics. *J. Materiomics* **2016**, *2*, 225−236.

(9) Glasser, L. Systematic Thermodynamics of Layered Perovskites: Ruddlesden-Popper Phases. *Inorg. Chem.* **2017**, *56*, 8920−8925.

(10) Rondinelli, J. M.; May, S. J.; Freeland, J. W. Control of octahedral connectivity in perovskite oxide heterostructures: An emerging route to multifunctional materials discovery. *MRS Bull.* **2012**, *37*, 261−270.

(11) Mulder, A. T.; Benedek, N. A.; Rondinelli, J. M.; Fennie, C. J. Turning ABO_3 Antiferroelectrics into Ferroelectrics: Design Rules for Practical Rotation-Driven Ferroelectricity in Double Perovskites and $A_3B_2O_7$ Ruddlesden-Popper Compounds. *Adv. Funct. Mater.* **2013**, *23*, 4810−4820.

(12) Rondinelli, J. M.; Poeppelmeier, K. R.; Zunger, A. Research Update: Towards designed functionalities in oxide-based electronic materials. *APL Mater.* **2015**, *3*, 080702.

(13) Rondinelli, J. M.; Kioupakis, E. Predicting and Designing Optical Properties of Inorganic Materials. *Annu. Rev. Mater. Res.* **2015**, *45*, 491−518.

(14) Benedek, N. A.; Rondinelli, J. M.; Djani, H.; Ghosez, P.; Lightfoot, P. Understanding ferroelectricity in layered perovskites: new ideas and insights from theory and experiments. *Dalton Trans.* **2015**, *44*, 10543−10558.

(15) Oh, Y. S.; Luo, X.; Huang, F.-T.; Wang, Y.; Cheong, S.-W. Experimental demonstration of hybrid improper ferroelectricity and the presence of abundant charged walls in $(Ca,Sr)_3Ti_2O_7$ crystals. *Nat. Mater.* **2015**, *14*, 407−413.

(16) Lu, X.-Z.; Rondinelli, J. M. Epitaxial-strain-induced polar-to-nonpolar transitions in layered oxides. *Nat. Mater.* **2016**, *15*, 951−955.

(17) Lu, X.-Z.; Rondinelli, J. M. Room Temperature Electric-Field Control of Magnetism in Layered Oxides with Cation Order. *Adv. Funct. Mater.* **2017**, *27*, 1604312.

(18) Udayakumar, K. R.; Cormack, A. N. Structural Aspects of Phase Equilibria in the Strontium-Titanium-Oxygen System. *J. Am. Ceram. Soc.* **1988**, *71*, C469−C471.

(19) McCoy, M. A.; Grimes, R. W.; Lee, W. E. Phase stability and interfacial structures in the SrO-$SrTiO_3$ system. *Philos. Mag. A* **1997**, *75*, 833−846.

(20) Noguera, C. Theoretical investigation of the Ruddlesden-Popper compounds $Sr_{n+1}Ti_nO_{3n+1}$(n = 1 − 3). *Philos. Mag. Lett.* **2000**, *80*, 173−180.

(21) Suzuki, T.; Fujimoto, M. First-principles structural stability study of nonstoichiometry-related planar defects in $SrTiO_3$ and $BaTiO_3$. *J. Appl. Phys.* **2001**, *89*, 5622−5629.

(22) Le Bacq, O.; Salinas, E.; Pisch, A.; Bernard, C.; Pasturel, A. First-principles structural stability in the strontium-titanium-oxygen system. *Philos. Mag.* **2006**, *86*, 2283−2292.

(23) Ramadan, A. H. H.; Allan, N. L.; De Souza, R. A. Simulation Studies of the Phase Stability of the Ruddlesden-Popper Phases. *J. Am. Ceram. Soc.* **2013**, *96*, 2316−2321.

(24) Jacob, K. T.; Rajitha, G. Thermodynamic properties of strontium titanates: Sr_2TiO_4, $Sr_3Ti_2O_7$, $Sr_4Ti_3O_{10}$, and $SrTiO_3$. *J. Chem. Thermodyn.* **2011**, *43*, 51−57.

(25) van Schilfgaarde, M.; Abrikosov, I. A.; Johansson, B. Origin of the Invar effect in iron-nickel alloys. *Nature* **1999**, *400*, 46−49.

(26) Yokoyama, T.; Eguchi, K. Anisotropic Thermal Expansion and Cooperative Invar and Anti-Invar Effects in Mn Alloys. *Phys. Rev. Lett.* **2013**, *110*, 075901.

(27) Padture, N. P.; Gell, M.; Jordan, E. H. Thermal Barrier Coatings for Gas-Turbine Engine Applications. *Science* **2002**, *296*, 280−284.

(28) Clarke, D. R.; Levi, C. G. Materials Design for the Next Generation Thermal Barrier Coatings. *Annu. Rev. Mater. Res.* **2003**, *33*, 383−417.

(29) Krost, A.; Dadgar, A. GaN-Based Devices on Si. *Phys. Status Solidi A* **2002**, *194*, 361−375.

(30) Han, J.-W.; Han, J.-M.; Kim, B.-Y.; Kim, Y.-H.; Kim, J.-H.; Seo, D.-S.; Park, Y.-P. Study on Compensation of Thermal Stresses in the Fabrication Process of Thin-Film Transistor. *Jpn. J. Appl. Phys.* **2008**, *47*, 2238.

(31) Lee, M.; Han, Y.; Um, H.; Choe, B. H.; Yim, T. H. Characteristics of electroformed low thermal expansion Fe-42wt.%Ni alloy substrates for thin film silicon solar cells. *J. Renewable Sustainable Energy* **2014**, *6*, 042008.

(32) Kino, H.; Hashiguchi, H.; Tanikawa, S.; Sugawara, Y.; Ikegaya, S.; Fukushima, T.; Koyanagi, M.; Tanaka, T. Effect of local stress induced by thermal expansion of underfill in three-dimensional stacked IC. *Jpn. J. Appl. Phys.* **2016**, *55*, 04EC03.

(33) Sai, N.; Vanderbilt, D. First-principles study of ferroelectric and antiferrodistortive instabilities in tetragonal $SrTiO_3$. *Phys. Rev. B: Condens. Matter Mater. Phys.* **2000**, *62*, 13942−13950.

DOI: 10.1021/acs.chemmater.8b02944
Chem. Mater. 2018, 30, 7100−7110

(34) Warusawithana, M. P.; Cen, C.; Sleasman, C. R.; Woicik, J. C.; Li, Y.; Kourkoutis, L. F.; Klug, J. A.; Li, H.; Ryan, P.; Wang, L.-P.; Bedzyk, M.; Muller, D. A.; Chen, L.-Q.; Levy, J.; Schlom, D. G. A Ferroelectric Oxide Made Directly on Silicon. *Science* **2009**, *324*, 367−370.
(35) Garcia, V.; Bibes, M. Ferroelectric tunnel junctions for information storage and processing. *Nat. Commun.* **2014**, *5*, 4289.
(36) Takenaka, K. Negative thermal expansion materials: technological key for control of thermal expansion. *Sci. Technol. Adv. Mater.* **2012**, *13*, 013001.
(37) Chen, J.; Hu, L.; Deng, J.; Xing, X. Negative thermal expansion in functional materials: controllable thermal expansion by chemical modifications. *Chem. Soc. Rev.* **2015**, *44*, 3522−3567.
(38) Barrera, G. D.; Bruno, J. A. O.; Barron, T. H. K.; Allan, N. L. Negative thermal expansion. *J. Phys.: Condens. Matter* **2005**, *17*, R217.
(39) Fultz, B. Vibrational thermodynamics of materials. *Prog. Mater. Sci.* **2010**, *55*, 247−352.
(40) Mittal, R.; Gupta, M. K.; Chaplot, S. L. Phonons and anomalous thermal expansion behaviour in crystalline solids. *Prog. Mater. Sci.* **2018**, *92*, 360−445.
(41) Hu, L.; Chen, J.; Fan, L.; Ren, Y.; Rong, Y.; Pan, Z.; Deng, J.; Yu, R.; Xing, X. Zero Thermal Expansion and Ferromagnetism in Cubic $Sc_{1-x}M_xF_3$ (M = Ga, Fe) over a Wide Temperature Range. *J. Am. Chem. Soc.* **2014**, *136*, 13566−13569.
(42) Huang, L.-F.; Zeng, Z. Roles of mass, structure, and bond strength in the phonon properties and lattice anharmonicity of single-layer Mo and W dichalcogenides. *J. Phys. Chem. C* **2015**, *119*, 18779−18789.
(43) Senn, M. S.; Murray, C. A.; Luo, X.; Wang, L.; Huang, F.-T.; Cheong, S.-W.; Bombardi, A.; Ablitt, C.; Mostofi, A. A.; Bristowe, N. C. Symmetry Switching of Negative Thermal Expansion by Chemical Control. *J. Am. Chem. Soc.* **2016**, *138*, 5479−5482.
(44) Hu, L.; Chen, J.; Xu, J.; Wang, N.; Han, F.; Ren, Y.; Pan, Z.; Rong, Y.; Huang, R.; Deng, J.; Li, L.; Xing, X. Atomic Linkage Flexibility Tuned Isotropic Negative, Zero, and Positive Thermal Expansion in $MZrF_6$ (M = Ca, Mn, Fe, Co, Ni, and Zn). *J. Am. Chem. Soc.* **2016**, *138*, 14530−14533.
(45) Hu, L.; et al. Localized Symmetry Breaking for Tuning Thermal Expansion in ScF_3 Nanoscale Frameworks. *J. Am. Chem. Soc.* **2018**, *140*, 4477−4480.
(46) Huang, L.-F.; Lu, X.-Z.; Rondinelli, J. M. Tunable Negative Thermal Expansion in Layered Perovskites from Quasi-Two-Dimensional Vibrations. *Phys. Rev. Lett.* **2016**, *117*, 115901.
(47) Huang, L.-F.; Lu, X.-Z.; Tennessen, E.; Rondinelli, J. M. An efficient ab-initio quasiharmonic approach for the thermodynamics of solids. *Comput. Mater. Sci.* **2016**, *120*, 84−93.
(48) Shirane, G. Neutron scattering studies of structural phase transitions at Brookhaven. *Rev. Mod. Phys.* **1974**, *46*, 437−449.
(49) Scott, J. F. Soft-mode spectroscopy: Experimental studies of structural phase transitions. *Rev. Mod. Phys.* **1974**, *46*, 83−128.
(50) Okai, B.; Yoshimoto, J. Pressure Dependence of the Structural Phase Transition Temperature in $SrTiO_3$ and $KMnF_3$. *J. Phys. Soc. Jpn.* **1975**, *39*, 162−165.
(51) Guennou, M.; Bouvier, P.; Kreisel, J.; Machon, D. Pressure-temperature phase diagram of $SrTiO_3$ up to 53 GPa. *Phys. Rev. B: Condens. Matter Mater. Phys.* **2010**, *81*, 054115.
(52) McCalla, E.; Walter, J.; Leighton, C. A Unified View of the Substitution-Dependent Antiferrodistortive Phase Transition in $SrTiO_3$. *Chem. Mater.* **2016**, *28*, 7973−7981.
(53) Hafner, J. Ab-initio simulations of materials using VASP: Density-functional theory and beyond. *J. Comput. Chem.* **2008**, *29*, 2044−2078.
(54) Perdew, J. P.; Ruzsinszky, A.; Csonka, G. I.; Vydrov, O. A.; Scuseria, G. E.; Constantin, L. A.; Zhou, X.; Burke, K. Restoring the Density-Gradient Expansion for Exchange in Solids and Surfaces. *Phys. Rev. Lett.* **2008**, *100*, 136406.
(55) Perdew, J. P.; Ruzsinszky, A.; Csonka, G. I.; Vydrov, O. A.; Scuseria, G. E.; Constantin, L. A.; Zhou, X.; Burke, K. Erratum: Restoring the Density-Gradient Expansion for Exchange in Solids and Surfaces [Phys. Rev. Lett. 100, 136406 (2008)]. *Phys. Rev. Lett.* **2009**, *102*, 039902.
(56) Blöchl, P. E. Projector augmented-wave method. *Phys. Rev. B: Condens. Matter Mater. Phys.* **1994**, *50*, 17953−17979.
(57) Kresse, G.; Joubert, D. From ultrasoft pseudopotentials to the projector augmented-wave method. *Phys. Rev. B: Condens. Matter Mater. Phys.* **1999**, *59*, 1758−1775.
(58) Shang, S.-L.; Wang, Y.; Kim, D.; Liu, Z.-K. First-principles thermodynamics from phonon and Debye model: Application to Ni and Ni_3Al. *Comput. Mater. Sci.* **2010**, *47*, 1040−1048.
(59) Kresse, G.; Furthmüller, J.; Hafner, J. Ab initio Force Constant Approach to Phonon Dispersion Relations of Diamond and Graphite. *Europhys. Lett.* **1995**, *32*, 729.
(60) Parlinski, K.; Li, Z. Q.; Kawazoe, Y. First-Principles Determination of the Soft Mode in Cubic ZrO_2. *Phys. Rev. Lett.* **1997**, *78*, 4063−4066.
(61) Togo, A.; Tanaka, I. First principles phonon calculations in materials science. *Scr. Mater.* **2015**, *108*, 1−5.
(62) Huang, L.-F.; Rondinelli, J. M. Electrochemical phase diagrams for Ti oxides from density functional calculations. *Phys. Rev. B: Condens. Matter Mater. Phys.* **2015**, *92*, 245126.
(63) Huang, L.-F.; Rondinelli, J. M. Stable $MoSi_2$ nanofilms with controllable and high metallicity. *Phys. Rev. Mater.* **2017**, *1*, 063001.
(64) Baroni, S.; De Gironcoli, S.; Dal Corso, A.; Giannozzi, P. Phonons and related crystal properties from density-functional perturbation theory. *Rev. Mod. Phys.* **2001**, *73*, 515−562.
(65) Wang, Y.; Shang, S.-L.; Fang, H.; Liu, Z.-K.; Chen, L.-Q. First-principles calculations of lattice dynamics and thermal properties of polar solids. *npj Comput. Mater.* **2016**, *2*, 16006.
(66) Shang, S.; Wang, Y.; Liu, Z.-K. First-principles calculations of phonon and thermodynamic properties in the boron-alkaline earth metal binary systems: B-Ca, B-Sr, and B-Ba. *Phys. Rev. B: Condens. Matter Mater. Phys.* **2007**, *75*, 024302.
(67) Shang, S.-L.; Zhang, H.; Wang, Y.; Liu, Z.-K. Temperature-dependent elastic stiffness constants of α-and θ-Al_2O_3 from first-principles calculations. *J. Phys.: Condens. Matter* **2010**, *22*, 375403.
(68) Baroni, S.; Giannozzi, P.; Isaev, E. Density-functional perturbation theory for quasi-harmonic calculations. *Rev. Mineral. Geochem.* **2010**, *71*, 39−57.
(69) Montanari, B.; Harrison, N. M. Pressure-induced instabilities in bulk TiO_2 rutile. *J. Phys.: Condens. Matter* **2004**, *16*, 273.
(70) Shojaee, E.; Mohammadizadeh, M. R. First-principles elastic and thermal properties of TiO_2: a phonon approach. *J. Phys.: Condens. Matter* **2010**, *22*, 015401.
(71) Mitev, P. D.; Hermansson, K.; Montanari, B.; Refson, K. Soft modes in strained and unstrained rutile TiO_2. *Phys. Rev. B: Condens. Matter Mater. Phys.* **2010**, *81*, 134303.
(72) Evarestov, R. A.; Blokhin, E.; Gryaznov, D.; Kotomin, E. A.; Maier, J. Phonon calculations in cubic and tetragonal phases of $SrTiO_3$: A comparative LCAO and plane-wave study. *Phys. Rev. B: Condens. Matter Mater. Phys.* **2011**, *83*, 134108.
(73) Ablitt, C.; Craddock, S.; Senn, M. S.; Mostofi, A. A.; Bristowe, N. C. The origin of uniaxial negative thermal expansion in layered perovskites. *npj Comput. Mater.* **2017**, *3*, 44.
(74) Ghosez, P.; Gonze, X.; Michenaud, J.-P. Coulomb interaction and ferroelectric instability of $BaTiO_3$. *Europhys. Lett.* **1996**, *33*, 713.
(75) Lu, Y.; Jia, D.; Gao, F.; Hu, T.; Chen, Z. First-principle calculations of the thermal properties of $SrTiO_3$ and $SrO(SrTiO_3)_n$ (n = 1,2). *Solid State Commun.* **2015**, *201*, 25−30.
(76) Anderson, O. L. A simplified method for calculating the debye temperature from elastic constants. *J. Phys. Chem. Solids* **1963**, *24*, 909−917.
(77) Moruzzi, V. L.; Janak, J. F.; Schwarz, K. Calculated thermal properties of metals. *Phys. Rev. B: Condens. Matter Mater. Phys.* **1988**, *37*, 790−799.
(78) Mei, Z.-G.; Shang, S.-L.; Wang, Y.; Liu, Z.-K. Density-functional study of the thermodynamic properties and the pressure-temperature phase diagram of Ti. *Phys. Rev. B: Condens. Matter Mater. Phys.* **2009**, *80*, 104116.

DOI: 10.1021/acs.chemmater.8b02944
Chem. Mater. 2018, 30, 7100−7110

(79) Hu, C. E.; Zeng, Z. Y.; Zhang, L.; Chen, X. R.; Cai, L. C.; Alfè, D. Theoretical investigation of the high pressure structure, lattice dynamics, phase transition, and thermal equation of state of titanium metal. *J. Appl. Phys.* **2010**, *107*, 093509.
(80) Shin, Y.; Jung, W.-S.; Lee, Y.-S. First-principles study on the thermal expansion of Ni-X binary alloys based on the quasi-harmonic Debye model. *Met. Mater. Int.* **2016**, *22*, 1065−1072.
(81) Feng, L.; Shiga, T.; Shiomi, J. Phonon transport in perovskite $SrTiO_3$ from first principles. *Appl. Phys. Express* **2015**, *8*, 071501.
(82) Tadano, T.; Tsuneyuki, S. Self-consistent phonon calculations of lattice dynamical properties in cubic $SrTiO_3$ with first-principles anharmonic force constants. *Phys. Rev. B: Condens. Matter Mater. Phys.* **2015**, *92*, 054301.
(83) Senn, M. S.; Bombardi, A.; Murray, C. A.; Vecchini, C.; Scherillo, A.; Luo, X.; Cheong, S. W. Negative Thermal Expansion in Hybrid Improper Ferroelectric Ruddlesden-Popper Perovskites by Symmetry Trapping. *Phys. Rev. Lett.* **2015**, *114*, 035701.
(84) Huang, L. F.; Gong, P. L.; Zeng, Z. Correlation between structure, phonon spectra, thermal expansion, and thermomechanics of single-layer MoS_2. *Phys. Rev. B: Condens. Matter Mater. Phys.* **2014**, *90*, 045409.
(85) Wallace, D. C. *Thermodynamics of Crystals*; Dover Publications, Inc.: New York, 1972.
(86) Schmerler, S.; Kortus, J. Ab initio study of AlN: Anisotropic thermal expansion, phase diagram, and high-temperature rocksalt to wurtzite phase transition. *Phys. Rev. B: Condens. Matter Mater. Phys.* **2014**, *89*, 064109.
(87) Arnaud, B.; Lebègue, S.; Raffy, G. Anisotropic thermal expansion of bismuth from first principles. *Phys. Rev. B: Condens. Matter Mater. Phys.* **2016**, *93*, 094106.
(88) Angel, R. J.; Zhao, J.; Ross, N. L. General Rules for Predicting Phase Transitions in Perovskites due to Octahedral Tilting. *Phys. Rev. Lett.* **2005**, *95*, 025503.
(89) Youssef, M.; Yildiz, B.; Van Vliet, K. J. Thermomechanical stabilization of electron small polarons in $SrTiO_3$ assessed by the quasiharmonic approximation. *Phys. Rev. B: Condens. Matter Mater. Phys.* **2017**, *95*, 161110.
(90) Cazorla, C.; Diéguez, O.; Íñiguez, J. Multiple structural transitions driven by spin-phonon couplings in a perovskite oxide. *Science Advances* **2017**, *3*, e1700288.
(91) Gryaznov, D.; Blokhin, E.; Sorokine, A.; Kotomin, E. A.; Evarestov, R. A.; Bussmann-Holder, A.; Maier, J. A Comparative Ab Initio Thermodynamic Study of Oxygen Vacancies in ZnO and $SrTiO_3$: Emphasis on Phonon Contribution. *J. Phys. Chem. C* **2013**, *117*, 13776−13784.
(92) Huang, L.-F.; Grabowski, B.; Zhang, J.; Lai, M.-J.; Tasan, C. C.; Sandlöbes, S.; Raabe, D.; Neugebauer, J. From electronic structure to phase diagrams: A bottom-up approach to understand the stability of titanium-transition metal alloys. *Acta Mater.* **2016**, *113*, 311−319.
(93) Galasso, F.; Darby, W. Preparation, structure, and properties of K_2NbO_3F. *J. Phys. Chem.* **1962**, *66*, 1318−1320.
(94) Kawamura, K.; Yashima, M.; Fujii, K.; Omoto, K.; Hibino, K.; Yamada, S.; Hester, J. R.; Avdeev, M.; Miao, P.; Torii, S.; Kamiyama, T. Structural Origin of the Anisotropic and Isotropic Thermal Expansion of K_2NiF_4-Type $LaSrAlO_4$ and Sr_2TiO_4. *Inorg. Chem.* **2015**, *54*, 3896−3904.
(95) Okazaki, A.; Kawaminami, M. Lattice constant of strontium titanate at low temperatures. *Mater. Res. Bull.* **1973**, *8*, 545−550.
(96) Liu, M.; Finlayson, T. R.; Smith, T. F. High-resolution dilatometry measurements of $SrTiO_3$salong cubic and tetragonal axes. *Phys. Rev. B: Condens. Matter Mater. Phys.* **1997**, *55*, 3480−3484.
(97) Huang, L.-F.; Gong, P.-L.; Zeng, Z. Phonon properties, thermal expansion, and thermomechanics of silicene and germanene. *Phys. Rev. B: Condens. Matter Mater. Phys.* **2015**, *91*, 205433.

DOI: 10.1021/acs.chemmater.8b02944
Chem. Mater. 2018, 30, 7100−7110